



HAL
open science

Frustration on a centred pyrochlore lattice in metal-organic frameworks

Rajah Nutakki, Richard Röss-Ohlenroth, Dirk Volkmer, Anton Jesche,
Hans-Albrecht Krug von Nidda, Alexander A. Tsirlin, Philipp Gegenwart,
Lode Pollet, L.D.C. Jaubert

► **To cite this version:**

Rajah Nutakki, Richard Röss-Ohlenroth, Dirk Volkmer, Anton Jesche, Hans-Albrecht Krug von Nidda, et al.. Frustration on a centred pyrochlore lattice in metal-organic frameworks. 2022. hal-03617124v1

HAL Id: hal-03617124

<https://hal.science/hal-03617124v1>

Preprint submitted on 30 Aug 2022 (v1), last revised 24 Apr 2023 (v2)

HAL is a multi-disciplinary open access archive for the deposit and dissemination of scientific research documents, whether they are published or not. The documents may come from teaching and research institutions in France or abroad, or from public or private research centers.

L'archive ouverte pluridisciplinaire **HAL**, est destinée au dépôt et à la diffusion de documents scientifiques de niveau recherche, publiés ou non, émanant des établissements d'enseignement et de recherche français ou étrangers, des laboratoires publics ou privés.

Frustration on a centred pyrochlore lattice in metal-organic frameworks

Rajah Nutakki,^{1,2} Richard Röß-Ohlenroth,³ Dirk Volkmer,³ Anton Jesche,⁴ Hans-Albrecht Krug von Nidda,⁵ Alexander A. Tsirlin,⁴ Philipp Gegenwart,⁴ Lode Pollet,^{1,2,6} and Ludovic D. C. Jaubert⁷

¹*Arnold Sommerfeld Center for Theoretical Physics,*

University of Munich, Theresienstr. 37, 80333 München, Germany

²*Munich Center for Quantum Science and Technology (MCQST), Schellingstr. 4, 80799 München, Germany*

³*Chair of Solid State and Materials Chemistry, Institute of Physics,*

University of Augsburg, D-86159 Augsburg, Germany

⁴*Experimental Physics VI, Center for Electronic Correlations and Magnetism,*

Institute of Physics, University of Augsburg, 86159 Augsburg, Germany

⁵*Experimental Physics V, Center for Electronic Correlations and Magnetism,*

Institute of Physics, University of Augsburg, 86159 Augsburg, Germany

⁶*Wilczek Quantum Center, School of Physics and Astronomy,*

Shanghai Jiao Tong University, Shanghai 200240, China

⁷*CNRS, Université de Bordeaux, LOMA, UMR 5798, 33400 Talence, France*

(Dated: March 17, 2022)

Geometric frustration inhibits magnetic systems from ordering, opening a window beyond Landau’s paradigm into topological matter and emergent gauge fields¹, with potential applications to quantum computing. In most systems frustration stems from one of only two elementary units of spins: either triangles^{2,3} or tetrahedra⁴. Here we explore an alternative route for frustration via molecular design in the metal-azolate framework [Mn(II)(ta)₂], whose units are *centred tetrahedra* made of five spins [Fig. 1]. Despite a Curie-Weiss temperature of -21 K indicating the energy scale of magnetic interactions, [Mn(II)(ta)₂] orders only at 0.43 K, putting it firmly in the category of highly frustrated magnets. Using a combination of simulations and field theory, we show that this material is proximate to a spin liquid described as a three-dimensional “slab” of a four-dimensional emergent electric field. The large degeneracy and robustness of this spin liquid, and additional chemical possibilities in the metal-organic frameworks beyond the pyrochlore structure, unlock a new door in frustrated magnetism.

Consider an elementary unit of frustration, labeled \mathcal{U}_n , made of n spins all coupled to each other antiferromagnetically. Most frustrated lattices are built by connecting these units together, with the notable exception of Kitaev systems⁵. \mathcal{U}_3 units are simple triangles, serving as the basis of many structures, such as kagome, triangular, square-kagome, hyperkagome or trillium lattices. The past 20 years have seen an explosion of experimental realisations of these lattices⁶, including ultracold atoms⁷, and Herbertsmithite, one of the most studied quantum spin liquids^{2,3}. As units grow larger, spins benefit from a broader manifold of degrees of freedom, providing enhanced stability to spin liquids⁸. This is especially true on the pyrochlore lattice, made of corner-sharing tetrahedra, \mathcal{U}_4 . Specific portions of this manifold can be selected by tuning the Hamiltonian with chemical substitution, magnetic field, and physical pressure^{4,9,10} to design the properties of the ground state; from hidden order^{11,12} to a wide range of spin liquids^{13–15}, passing by magnetisation plateaux^{16,17} and fragmentation^{18,19}. But it is probably in spin ice^{20,21} that this design takes its most elegant form, with the emergence of a Coulomb gauge field and magnetic monopoles²².

However, although the same breadth of phenomena is expected for $\mathcal{U}_{n \geq 5}$, comparatively little is known about them. A complication is that triangles and tetrahedra are not easily extended to \mathcal{U}_5 : It is impossible to put five sites at equidistance from each other in 3D – a point we come back to later. But this mathematical conundrum can be circumvented with a bit of chemical cunning. Metal-organic frameworks are a class of crystalline materials, where metal ions are connected by organic linkers, offering a high

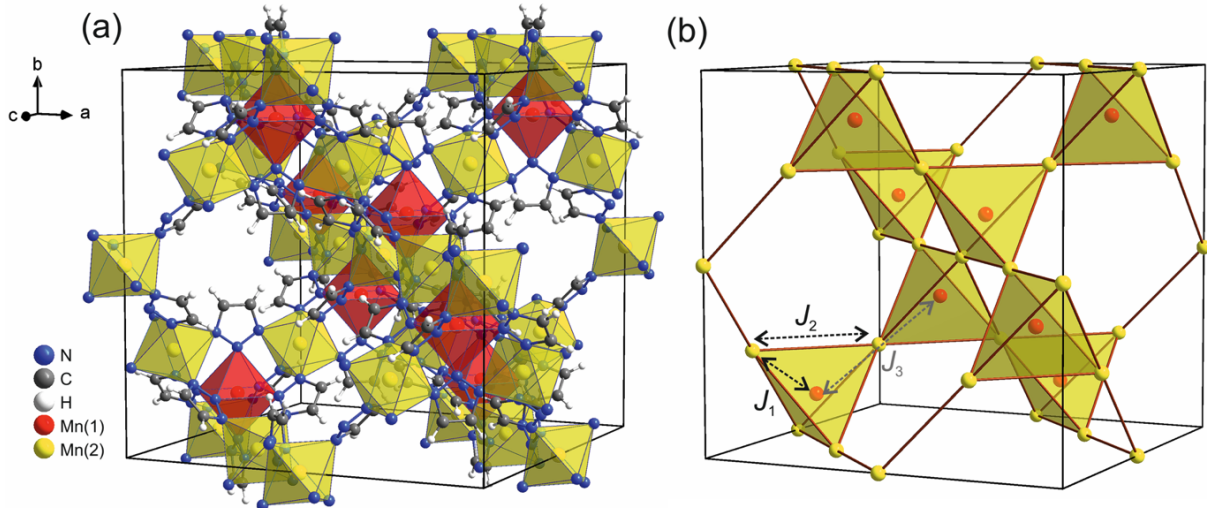


FIG. 1. **Metal-azolate framework & centred pyrochlore lattice.** **a**, Combined ball-and-stick and polyhedra model of cubic $[\text{Mn(II)}(\text{ta})_2]$ highlighting the positions of divalent octahedrally coordinated Mn ions arranged in a diamond-type lattice (CSD code: HEJQEV). The metal centres differ with respect to their special crystallographic positions and coordination environments: Mn(1) is located on Wyckoff position 8b (site symmetry $\bar{4}3m$), coordinated exclusively by the N2 donor atoms of the μ_3 -bridging triazolate linker; Mn(2) is found at Wyckoff position 16d (site symmetry $\bar{3}m$), coordinated exclusively by N1 or N3 donor atoms. **b**, Schematic representation of the centred pyrochlore lattice with magnetic exchange paths for first (J_1 , Mn(1)–Mn(2), 3.929Å), second (J_2 , Mn(2)–Mn(2), 6.416Å) and third (J_3 , Mn(1)–Mn(1), 7.858Å) neighbours. Mn(1) and Mn(2) are respectively labeled centre (orange) and corner (yellow) spins.

degree of tunability. The metal-azolate frameworks $[\text{M(II)}(\text{ta})_2]$, where M(II) is a divalent metal ion and H-ta = 1H-1,2,3-triazole, is especially promising in that respect. Early studies for $\text{M} = \{\text{Cd}, \text{Mg}, \text{Mn}, \text{Fe}, \text{Co}, \text{Cu}, \text{Zn}\}$ ^{23,24} showed a diamond net with vertices made of M-centred (MM_4) tetrahedra [Fig. 1]. The above conundrum is thus sidestepped by placing the fifth magnetic ion in the centre of the tetrahedron, thereby forming a \mathcal{U}_5 unit where all five spins are coupled to each other. The exciting possibility to engineer magnetic exchange interactions by inserting additional, magnetically active ions into the iconic pyrochlore network is very appealing, but only a handful of works have addressed their magnetic properties^{24–28}.

Model and simulation methods. Among the metal-azolate frameworks, we chose to study $[\text{Mn}(\text{ta})_2]$ for its particularly high symmetry. Adapting the synthesis procedure of Ref. [29], $[\text{Mn}(\text{ta})_2]$ was prepared as a white powder sample. Rietveld refinements of X-ray diffraction data found that $[\text{Mn}(\text{ta})_2]$ has the cubic symmetry of the $Fd\bar{3}m$ space group²⁴ that we confirmed through X-ray powder diffraction at 5 K. The 3d valence band of high-spin Mn(II) ions being half filled, its magnetic moment is essentially isotropic. Previous conductivity measurements together with periodic DFT band structure calculations³⁰ classified this compound as a wide-bandgap semiconductor with a bandgap $\Delta = 3.1 \text{ eV} \equiv 36000 \text{ K}$. We therefore effectively consider $[\text{Mn}(\text{ta})_2]$ an insulator at temperatures $T \ll \Delta$.

To assess the relevance of different exchange pathways [Fig. 1], we performed DFT calculations assuming isotropic exchanges for high-spin 3d⁵ Mn(II) ions between first (J_1), second (J_2) and third (J_3) neighbours [see Fig. 1.b and Supplementary Information]. We obtain that $J_1^{\text{DFT}} \sim 2 - 4 \text{ K}$ and despite the difference in distances between first (3.93 Å) and second (6.42 Å) neighbours, J_1^{DFT} and J_2^{DFT} are of the same order: $\gamma^{\text{DFT}} \equiv J_1^{\text{DFT}}/J_2^{\text{DFT}} \approx 1.3 - 1.65$. This is probably because of the similar exchange pathways, traversing either two or three nitrogen ions respectively along the triazolate ligand. On the other hand, no such pathway is available beyond second J_2 neighbours, hence $|J_3^{\text{DFT}}| < 0.01 \text{ K} \ll J_1^{\text{DFT}}, J_2^{\text{DFT}}$. This is why we define our CPy model on the centred pyrochlore lattice with first and second neighbour isotropic

couplings, which is equivalent to a $J_1 - J_2$ decorated diamond lattice,

$$H = J_1 \sum_{\langle ij \rangle} \mathbf{S}_i \cdot \mathbf{S}_j + J_2 \sum_{\langle\langle ij \rangle\rangle} \mathbf{S}_i \cdot \mathbf{S}_j - \mu_0 \mathbf{H} \cdot \sum_i \mathbf{S}_i \quad (1)$$

In order to confirm that $[\text{Mn}(\text{ta})_2]$ is described by Hamiltonian (1), we need to find the appropriate theoretical tools. Numerical investigations are hindered by the fact that quantum Monte Carlo simulations suffer from the infamous sign-problem that plagues most quantum frustrated models. Fortunately, the large magnetic moment $S = 5/2$ justifies a classical approach. Classical Monte Carlo simulations have proven powerful techniques to describe magnetic properties of pyrochlore materials, from long-range order to the unconventional correlations of spin liquids^{10,14,21,31-33}, and will be our method of choice here. Continuous-spin models cannot, however, reproduce specific heat at very low temperatures because entropy is ill defined. There, one needs to consider the discrete nature of quantum spins via e.g. exact diagonalisation (ED). Since ED for $S = 5/2$ is particularly costly in computer time and memory, we will restrict calculations to a single unit \mathcal{U}_5 of five spins, fitted to high-temperature experimental data. Such approximation shall provide an independent estimate of the energy scales at play, to be compared with parameters obtained from DFT and Monte Carlo simulations. This is why in the rest of this paper, \mathbf{S}_i will denote a 3-component classical spin of length $|\mathbf{S}_i| = 5/2$, except when analysing specific-heat data where \mathbf{S}_i is a quantum spin $S = 5/2$.

Comparisons between experiment & theory. Fitting the high-temperature regime ($T > 200$ K) of susceptibility χ with a Curie-Weiss law [Fig. 2.a], we obtain an effective magnetic moment $\mu_{\text{eff}} = 6.05 \mu_B$ per Mn ion and a Curie-Weiss temperature $\Theta_{CW} = -21$ K. These values agree with a previous report²⁴ ($5.8 \mu_B$ and -21.9 K respectively) and with the expected size of the magnetic moment $g_S \sqrt{S(S+1)} = 5.9 \mu_B$ for a high-spin $3d^5$ electronic configuration. Θ_{CW} indicates sizeable antiferromagnetic interactions, but our specific heat measurements reveal no transition down to $T_c = 0.43$ K [Fig. 2.d]. As a point of comparison, its degree of frustration $f \equiv \frac{|\Theta_{CW}|}{T_c} = 49$ is of the same order than Kitaev materials^{34,35} and substantially larger than most rare-earth pyrochlore oxides^{4,21,36}. It means that not only does $[\text{Mn}(\text{ta})_2]$ present a yet unexplored geometry, but we can expect a sizeable temperature range above T_c with original, frustrated, physics.

One of our main result is the quantitative agreement between experiments and Monte Carlo simulations for (i) the magnetic susceptibility in Fig. 2.a,b, and (ii) magnetisation curves in Fig. 2.c, using coupling parameters $J_1^{\text{MC}} = 2.0$ K and $\gamma^{\text{MC}} = 1.51 \pm 0.15$. The bump in specific heat at ~ 4 K is also consistent with finite-temperature exact diagonalisation for $J_1^{\text{ED}} = 1.95$ K and $\gamma^{\text{ED}} \sim 1.75$ [Fig. 2.d]. While the value of γ^{ED} should only be considered as a qualitative estimate, ED results indicate that the bump at 4 K corresponds to a growth of the correlation length beyond a single frustrated unit. The region $0.43 < T \lesssim 4$ K thus appears appropriate to support a potentially exotic magnetic texture, where frustrated correlations have taken place, but before they are destroyed by long-range order.

Note that Monte Carlo simulations show no sign of magnetic order for this range of parameters. It means that the ordering mechanism in $[\text{Mn}(\text{ta})_2]$ lies beyond our minimal CPy model. This is often the case in frustrated magnetism^{4,21,35,36}, where perturbations ultimately lift the ground-state degeneracy in materials. Familiar culprits are further-neighbour coupling or anisotropic exchange. To discover the nature of this magnetic order would be a separate project in itself and is beyond the scope of this paper, where we want to understand what kind of magnetic texture lies above T_c .

As a rolling summary, $[\text{Mn}(\text{ta})_2]$ is properly described by the microscopic CPy model of Hamiltonian (1) above its ordering temperature T_c . An estimate of $\gamma_{\text{exp}} = 1.55 \pm 0.20$ is consistent with three independent methods: ab-initio DFT, Monte Carlo simulations fitted to magnetic measurements and ED fitted to specific heat. Neutron scattering would have been a useful probe to investigate magnetic correlations experimentally, but neutrons are absorbed by hydrogen atoms, a common issue for organic compounds. In absence of a deuterated version of $[\text{Mn}(\text{ta})_2]$, we will study the phase diagram of Hamiltonian (1)

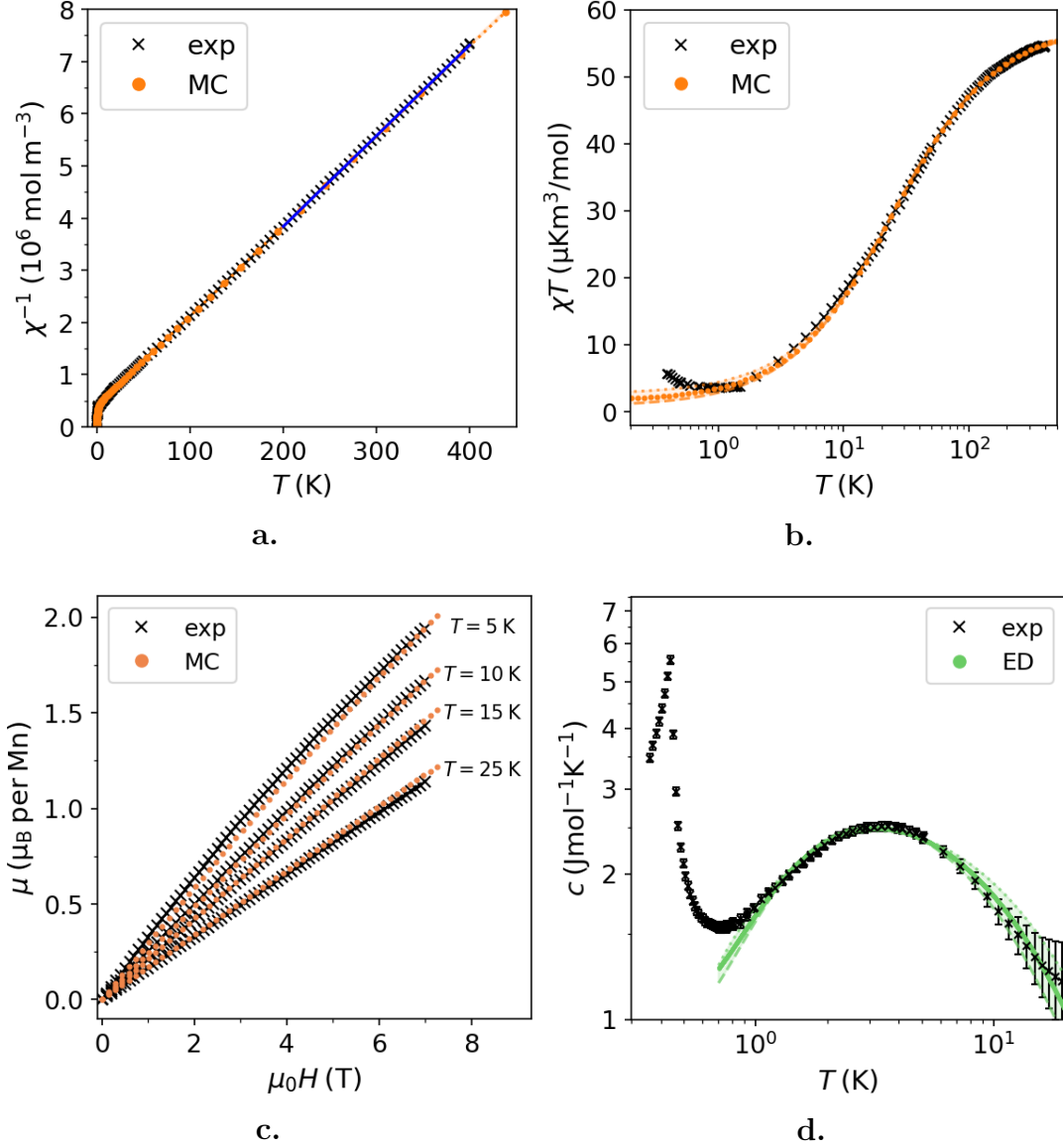


FIG. 2. **Comparison between experiment and theory for $[\text{Mn}(\text{ta})_2]$.** **a**, Curie-Weiss fit (blue, for $T > 200$ K) of the inverse susceptibility χ^{-1} obtained from magnetisation measurements $\chi = M/H$ (black). Experimental and Monte-Carlo data compare quantitatively well for the susceptibility (**a,b**) and magnetisation curves in a magnetic field H (**c**), for $J_1^{\text{MC}} = 2.0$ K, $\gamma^{\text{MC}} = 1.51 \pm 0.15$ [Eq. (1)]. The Landé factor is $g = 2.05$ obtained from the Curie-Weiss fit. **d**, Specific heat of $[\text{Mn}(\text{ta})_2]$ displays a broad bump at ~ 4 K and a sharp peak at 0.43 K. The former is qualitatively reproduced by finite-temperature exact diagonalisation for $J_1^{\text{ED}} = 1.95$ K and $\gamma^{\text{ED}} \sim 1.75$ up to a rescaling by a factor of 0.8 along the y -axis. In order to show the γ dependence of Hamiltonian (1), theoretical curves in b and d are supplemented by dotted and dashed lines corresponding to $\pm 10\%$ variations of γ .

theoretically, focusing on the experimentally relevant parameter region.

Phase diagram. In Eq. (1), negative and positive values of J_1 are equivalent by a global π rotation of all centre spins; for $J_2 < 0$ the system orders into a trivial ferro- or ferri-magnet respectively. Hence we shall restrict our attention to (experimentally relevant) antiferromagnetic couplings $J_1, J_2 > 0$. To derive

its phase diagram, it is convenient to rewrite Hamiltonian (1) as a sum over \mathcal{U}_5 units, with index α ,

$$H = \frac{J_2}{2} \sum_{\alpha} |\mathbf{L}_{\alpha}|^2 + \text{const}, \quad (2)$$

$$\text{with } \mathbf{L}_{\alpha} = \gamma \mathbf{S}_{\alpha,c} + \sum_{m=1}^4 \mathbf{S}_{\alpha,m}, \quad (3)$$

where c labels the centre spin while the sum over m runs over the four corner spins. The ground state manifold is defined by minimising $L_{\alpha} = |\mathbf{L}_{\alpha}|$ on all units. For $\gamma \geq 4$, it gives a ferrimagnet with $1/3$ saturated magnetisation where $\mathbf{S}_{\alpha,i=1,\dots,4} = -\mathbf{S}_{\alpha,c}$ [Fig. 3.a]. On the other hand, for $\gamma < 4$, the ground state is defined by the local constraint

$$L_{\alpha} = 0, \quad \forall \alpha. \quad (4)$$

Ferrimagnetic order smoothly vanishes with γ , until it turns into a spin liquid. Remarkably, this magnetically disordered ground state is stable over a broad parameter range, $0 \leq \gamma \lesssim 3$ [Fig. 3.a].

Let us put this spin liquid in a broader picture with respect to lattice counterparts made of smaller units: the kagome (\mathcal{U}_3) and pyrochlore (\mathcal{U}_4) Heisenberg antiferromagnets (HAF) where constraint (4) also holds in the ground state, albeit with only 3 and 4 spins respectively in Eq. (3). Magnetisation can be rewritten as an effective field with zero divergence, i.e. whose flux is conserved, as for an electric field in Maxwell's equations²¹. This is why constraint (4) is known to support an emergent Coulomb spin liquid on kagome and pyrochlore. A Maxwellian counting argument⁸ gives the degrees of freedom D_n for these spin liquids, and how it scales with the number of units N_u . It is $D_3 = 0$ for kagome (which is famously marginally disordered) and $D_4 = N_u$ for pyrochlore⁸. Similarly, these spin liquids manifest themselves via a number of flat bands F_n as the ground state of their excitation spectrum³⁷: $F_3 = 1$ out of 3 bands for kagome, $F_4 = 2$ out of 4 for pyrochlore.

On the CPy model, we find $D_5 = 3 N_u$ for $\gamma \sim 1$ and $F_5 = 4$ flat bands out of 6 for $\gamma < 4$. Our point is that the CPy model supports a notably strong spin liquid, even more disordered than the extensively studied ones on kagome and pyrochlore. Since parameters of $[\text{Mn}(\text{ta})_2]$ are in the middle of this disordered ground state, $0 \leq \gamma_{\text{exp}} \lesssim 3$, we expect the spin-liquid regime to persist in the temperature window, $0.43 < T \lesssim 4$ K. But to describe its magnetic texture, is it possible to derive a similar analogy to a Coulomb field ?

A glimpse into the 4th dimension. Magnetic correlations are best visualised through the structure factor in reciprocal space, $\mathcal{S}(\mathbf{q})$, obtained from simulations [Fig. 3.b-d]. From the phase diagram [Fig. 3.a], we have two asymptotic regimes. As $\gamma \rightarrow 3^-$ short-range ferrimagnetic correlations dominate [Fig. 3.d], while for $\gamma \rightarrow 0^+$ the pyrochlore HAF is recovered, decoupled from the paramagnetic centre spins. Pinch points are already visible for $\gamma = 1/3$ [Fig. 3.b], signalling the 3D Coulomb gauge field of the pyrochlore HAF^{21,38}. There are no singularities between these two limits, which means that the magnetic textures continuously evolve from one to the other. In particular pinch points are diffuse for $\gamma = 1.54$ [Fig. 3.c] despite the apparent zero-divergence constraint (4) to support them.

This is where we should step back and remember that five points cannot be equidistant in 3D. But in 4D, they can. The trick is to perform a Gedankenexperiment where we pull out the centre spin into a 4th dimension, expanding the reference frame to (x, y, z, t) . Fig. 3.f illustrates this idea from 2D to 3D, and mathematical details are given in the Supplementary Information. In a nutshell, the CPy model is mapped onto a slab where all corner spins belong to hyperplane t , while centre spins are shifted to $t \pm \delta t$ layers alternatively, respecting the bipartiteness of the underlying diamond net. Through this mapping the \mathcal{U}_5 unit becomes a full-fledged pentachoron, the 4D analogue of a tetrahedron; the centred tetrahedron is actually a standard Schlegel diagram – a common representation of 4D objects – of a pentachoron.

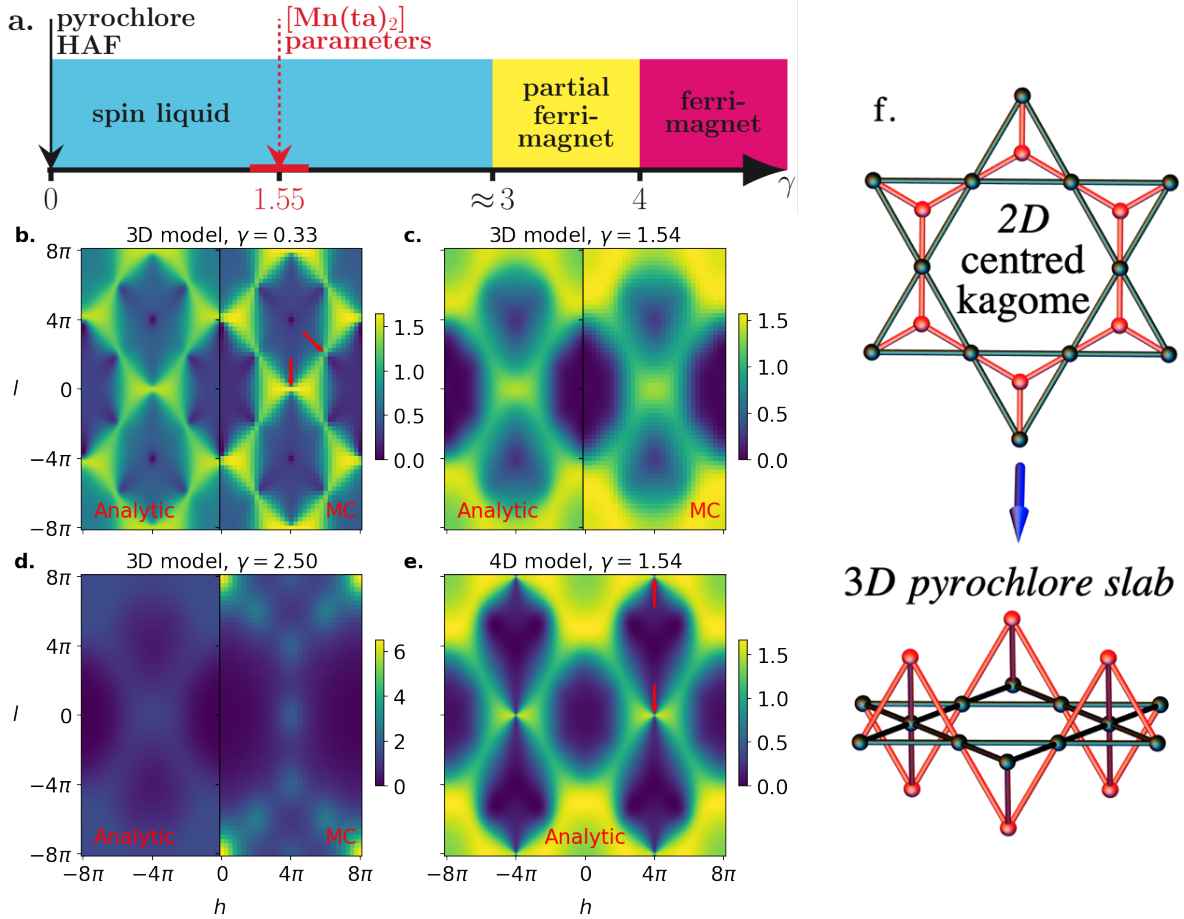


FIG. 3. **Phase diagram & 4D Coulomb field.** **a**, Phase diagram of the CPy model at $T \rightarrow 0^+$ obtained from simulations, and indicating the parametrisation γ_{exp} of $[\text{Mn}(\text{ta})_2]$. **b-d**, Structure factor $\mathcal{S}(\mathbf{q})$ of the 3D CPy model in the $[\text{hhl}]$ plane calculated from field theory (left half) and simulations (right half) for $\gamma = \{0.33, 1.54, 2.5\}$. Pinch points are marked by arrows. Note that the maximum intensity in simulations is higher close to ferrimagnetic order in panel d. **e**, Structure factor of the 4D pentachore model in the $[\text{hhl}0]$ plane calculated from field theory. Note that only some of the 4D pinch points are visible in the physically relevant $[\text{hhl}0]$ reciprocal plane since the position of Brillouin zone centres shift from 3D to 4D. **f**, Illustration of the mapping from the 3D CPy model to the 4D “pentachore” lattice in lower dimensions; a centred kagome lattice becomes a $[111]$ slab of the pyrochlore lattice by shifting the centre sites of triangles alternately up and down.

To test this idea, we develop a field theory of the spin liquid on the CPy model that can be extended to a 4D lattice made of corner-sharing pentachora. This method quantitatively reproduces the simulated structure factor for $\gamma \lesssim 2$ in 3D [Fig. 3.b,c], away from the $\gamma \rightarrow 3^-$ limit because the onset of ferrimagnetic order is not properly captured by our field theory. The Gedankenexperiment is confirmed since the diffuse features of the 3D CPy model become sharp pinch points in 4D [Fig. 3.e]. Hence, the broadened pinch points observed in 3D are a consequence of the underlying, hidden, slab geometry of the CPy model; the centre spins are effectively lying on hyperplanes in 4D with open boundaries, where the magnetisation flux can locally exit the lattice.

Outlook. The CPy model supports a robust spin liquid with a huge number of degrees of freedom, more than most known spin liquids. Inspired by what has been done on pyrochlores^{4,9,10}, Hamiltonian (1) offers a pristine foundation on which to build a plethora of exotic phases, taking a selection of degrees of freedom out of the ground state, e.g. via chemical substitution, magnetic field, physical and chemical pressure. $[\text{Mn}(\text{ta})_2]$ belongs to a broader family of metal-azolate frameworks, providing a versatile platform to engineer frustrated magnetism on the CPy model and beyond, such as $[\text{Fe}(\text{ta})_2(\text{BF}_4)_x]$ with a degree of frustration $f \approx 27$ ²⁶ and $[\text{Cu}(\text{ta})_2]$ with Cu(II) dimers at low temperature²⁵. Large exchange couplings can be manufactured with appropriate ligands as well²⁸. A rich diversity of unconventional frustrated properties are yet to be explored in metal-organic frameworks.

Even if $[\text{Mn}(\text{ta})_2]$ is necessarily three dimensional, our model provides a glimpse of what a spin liquid would look like in higher dimensions; it provides a way to rationalise complex many-body physics into a simpler emergent phenomena. Consequences of this 4D picture on the inelastic spectrum, nature of excitations and quantum fluctuations are promising open questions. Possibilities are numerous for molecular designs, experimental characterisation and theoretical developments.

Acknowledgements We are grateful to Nic Shannon for stimulating discussions. D.V. and R.R.-O. are grateful for financial support from DFG grant VO-829/12-2 (DFG Priority Program 1928 “Coordination Networks: Building Blocks for Functional Systems”) and SEM micrographs taken by Ralph Freund. A.A.T., A.J., P.G., and H.-A. K.v.N. were supported by the German Research Foundation via TRR80. L.D.C.J. acknowledges financial support from the “Agence Nationale de la Recherche” under Grant No.ANR-18-CE30-0011-01. R.N., L.P. and L.D.C.J. acknowledge financial support from the LMU-Bordeaux Research Cooperation Program. R. N. and L. P. acknowledge support from FP7/ERC Consolidator Grant QSIMCORR, No. 771891, and the Deutsche Forschungsgemeinschaft (DFG, German Research Foundation) under Germany’s Excellence Strategy – EXC-2111 – 390814868. Our simulations make use of the ALPSCore library³⁹.

Author contributions R.R.-O. performed the synthesis and analytical characterization of the metal azolate compounds. D.V. developed the concept and designed experiments. A.J. performed thermodynamic measurements and analysed their results together with P.G. and H.-A. K.v.N. A.A.T. performed DFT calculations. R.N. performed the Monte-Carlo simulations and field-theory calculations. L.P. and L.D.C.J. directed the theory part of the project. All authors contributed critically to the writing of the manuscript and the interpretation of the experimental and numerical results.

Competing interests The authors declare no competing interests.

METHODS

General Synthetic Method $[\text{Mn}(\text{ta})_2]$ and $[\text{Zn}(\text{ta})_2]$ were prepared by procedures adapted from literature²⁴ and characterised by IR-spectroscopy, x-ray powder diffraction (XRPD) and electron microscopy [Supplementary Information]. The synthesis of $[\text{Mn}(\text{ta})_2]$ was conducted twice in order to re-evaluate the magnetic properties and rule out batch effects. We have also performed the high-resolution synchrotron XRPD measurement at 5 K to ensure that the crystal symmetry remains cubic down to low temperatures.

Magnetic measurements A Quantum Design MPMS3 magnetometer equipped with an iQuantum He3 option was employed to measure the magnetisation at temperatures of $T = 0.4 - 400$ K in applied fields $\mu_0 H = 0.02$ T below 20 K, and 7 T above 20 K. 20K was chosen as a good compromise between the increasing noise/signal ratio of the 20mT data at higher temperatures, and deviations from the linear regime at 7T at lower temperatures. Fig. 2.c confirms that we are in the linear regime up to 7T. The powder was mounted using a plastic capsule that was also measured empty in order to determine the background contribution for $T > 2$ K. The error of the absolute value of the measured magnetic moment in the He3 region ($T < 2$ K) is larger than the one at higher temperatures ($T > 2$ K). Therefore, a small offset ($\sim 5\%$ of the absolute value, which is smaller than the size of the data points in Fig. 2.b) was subtracted from the He3 data such that it fits the susceptibility obtained at $T = 2$ K.

Specific-heat measurements Specific heat was measured on a pressed pellet by a relaxation method using Quantum Design PPMS with the He3 insert. In order to determine non-magnetic contributions, the specific heat of the non-magnetic analogue $[\text{Zn}(\text{ta})_2]$ was measured in the full temperature range. For $T < 1.8$ K, the magnetic contribution was found to amount to more than 99.7% of the absolute value

and the non-magnetic host is negligible. For increasing temperatures to $T > 2$ K the latter becomes more important and has to be subtracted to get reliable values for C_{mag} . To this extend, the temperature axis of the $[\text{Zn}(\text{ta})_2]$ for $C(T)$ had to be re-scaled to account for a different Debye temperature; a factor of 0.91 was applied such that specific heat of $[\text{Mn}(\text{ta})_2]$ and $[\text{Zn}(\text{ta})_2]$ approach identical values at $T \approx 50$ K.

Density-functional calculations were performed in the FPLO code⁴⁰ using the experimental crystal structure of $[\text{Mn}(\text{ta})_2]$ ²⁹. Magnetic exchange couplings defined in Eq. (1) with $S = 5/2$ of Mn^{2+} were obtained by a mapping procedure⁴¹, with total energies of individual spin configurations converged on a k -mesh with 64 points in the first Brillouin zone. The Perdew-Burke-Ernzerhof exchange-correlation potential⁴² was used, and correlations effects in the Mn 3d shell were taken into account of the mean-field DFT+ U level with the on-site Coulomb repulsion parameter $U_d = 5$ eV and Hund's coupling $J_H = 1$ eV. This choice of parameters not only led to a good agreement with the experiment, but also showed consistency with the previous ab initio calculations for other Mn^{2+} frustrated magnets⁴³. Additionally, we varied the U_d value in a broad range to ensure that the resulting γ is not significantly affected by this parameter. Details can be found in the Supplemental Information.

Monte Carlo Simulations Simulations were performed for cubic $L \times L \times L$ systems with periodic boundary conditions. L is the number of conventional cubic unit cells in x , y and z directions, giving a total of $N = 24L^3$ spins. We used single-spin heat-bath⁴⁴⁻⁴⁶ and over-relaxation⁴⁶⁻⁴⁹ updates, with one MC step made up of a sweep of both updates through the entire lattice. Simulations were typically performed using a minimum of 10^5 thermalization and measurement steps, increasing up to a maximum of 10^7 thermalization and measurement steps to access lower temperatures. In each MC measurement step, we calculated the magnetisation,

$$\mathbf{m} = \frac{1}{N} \left\langle \sum_i \mathbf{S}_i \right\rangle, \quad (5)$$

where $\mathbf{m} = (m_x, m_y, m_z)^T$, and magnetic susceptibility (per site) along a single axis

$$\chi_z = \frac{N}{T} \left(\langle m_z^2 \rangle - \langle m_z \rangle^2 \right), \quad (6)$$

for system sizes up to $L = 12$. We also computed the static spin structure factor,

$$\mathcal{S}(\mathbf{q}) = \frac{1}{N} \sum_{j,k} e^{i\mathbf{q} \cdot (\mathbf{r}_j - \mathbf{r}_k)} \langle \mathbf{S}_j \cdot \mathbf{S}_k \rangle, \quad (7)$$

every 100 MC measurement steps, for system sizes up to $L = 10$. \mathbf{r}_j is the vector position of site j .

For comparison to experiments, the magnetisation m_z and susceptibility χ_z were scaled by $(1 + 1/S) = 1.4$ to account for the difference between classical continuous spins and quantum spins $S = 5/2$.

Analytical Methods We employed the generalized Luttinger-Tisza method⁵⁰, for finding exact ground states in momentum space. In particular, we obtained that the ground state of the CPy model for $\gamma < 4$ corresponds to a four-fold degenerate flat band.

The degeneracy of the four flat bands for $\gamma < 4$ was also obtained by adapting the argument of Refs. [51,52] for the centred pyrochlore geometry. Hamiltonian (2) can be rewritten as a product of rectangular matrices whose rank scales at most with the number of central spins, $N/3$. It means that the kernel of the Hamiltonian is at least of dimension $(N - N/3) = 2N/3$; hence $2/3$ of the 6 bands are flat.

To calculate the $T = 0$ static spin structure factor for the CPy model and its 4D analogue on the pentachore lattice, we adapted the calculation presented in Ref. [53], where one projects onto the subspace satisfying the momentum space representation of the local constraint.

Exact Diagonalisation Full diagonalization of the Hamiltonian was performed on a single tetrahedron consisting of five $S = \frac{5}{2}$ quantum spins with open boundary conditions. The specific heat (per tetrahedron) was calculated from the resulting energy spectrum using

$$C = \frac{1}{T^2} (\langle E^2 \rangle - \langle E \rangle^2) \quad (8)$$

where $\langle \dots \rangle$ is the finite temperature equilibrium expectation value at temperature T . Results for various γ were compared to experiment using the energy scale, J_1 , and a rescaling factor for C as free parameters.

- ¹ J. Knolle and R. Moessner, [Annual Review of Condensed Matter Physics](#) **10**, 451 (2019).
- ² M. R. Norman, [Rev. Mod. Phys.](#) **88**, 041002 (2016).
- ³ P. Mendels and F. Bert, [Comptes Rendus Physique](#) **17**, 455 (2016).
- ⁴ J. G. Rau and M. J. Gingras, [Annual Review of Condensed Matter Physics](#) **10**, 357 (2019).
- ⁵ M. Hermanns, I. Kimchi, and J. Knolle, [Annual Review of Condensed Matter Physics](#) **9**, 17 (2018).
- ⁶ C. Broholm, R. J. Cava, S. A. Kivelson, D. G. Nocera, M. R. Norman, and T. Senthil, [Science](#) **367**, eaay0668 (2020).
- ⁷ G.-B. Jo, J. Guzman, C. K. Thomas, P. Hosur, A. Vishwanath, and D. M. Stamper-Kurn, [Phys. Rev. Lett.](#) **108**, 045305 (2012).
- ⁸ R. Moessner and J. T. Chalker, [Physical Review B](#) **58**, 12049 (1998).
- ⁹ K. A. Ross, L. Savary, B. D. Gaulin, and L. Balents, [Phys. Rev. X](#) **1**, 021002 (2011).
- ¹⁰ H. Yan, O. Benton, L. D. C. Jaubert, and N. Shannon, [Phys. Rev. B](#) **95**, 094422 (2017).
- ¹¹ H. Takatsu, S. Onoda, S. Kittaka, A. Kasahara, Y. Kono, T. Sakakibara, Y. Kato, B. Fåk, J. Ollivier, J. W. Lynn, T. Taniguchi, M. Wakita, and H. Kadowaki, [Phys. Rev. Lett.](#) **116**, 217201 (2016).
- ¹² R. Sibille, N. Gauthier, E. Lhotel, V. Porée, V. Pomjakushin, R. A. Ewings, T. G. Perring, J. Ollivier, A. Wildes, C. Ritter, T. C. Hansen, D. A. Keen, G. J. Nilsen, L. Keller, S. Petit, and T. Fennell, [Nature Physics](#) **16**, 546 (2020).
- ¹³ O. Benton, L. D. C. Jaubert, H. Yan, and N. Shannon, [Nature Communications](#) **7**, 11572 (2016).
- ¹⁴ S. Zhang, H. J. Changlani, K. W. Plumb, O. Tchernyshyov, and R. Moessner, [Physical Review Letters](#) **122**, 167203 (2019).
- ¹⁵ C. Liu, G. B. Halász, and L. Balents, [Phys. Rev. B](#) **104**, 054401 (2021).
- ¹⁶ K. Matsuhira, Z. Hiroi, T. Tayama, S. Takagi, and T. Sakakibara, [Journal of Physics-Condensed Matter](#) **14**, L559 (2002).
- ¹⁷ K. Penc, N. Shannon, and H. Shiba, [Phys. Rev. Lett.](#) **93**, 197203 (2004).
- ¹⁸ M. E. Brooks-Bartlett, S. T. Banks, L. D. C. Jaubert, A. Harman-Clarke, and P. C. W. Holdsworth, [Phys. Rev. X](#) **4**, 011007 (2014).
- ¹⁹ S. Petit, E. Lhotel, B. Canals, M. Ciomaga Hatnean, J. Ollivier, H. Mutka, E. Ressouche, A. R. Wildes, M. R. Lees, and G. Balakrishnan, [Nature Physics](#) **12**, 746 (2016).
- ²⁰ M. J. Harris, S. T. Bramwell, D. F. McMorrow, T. Zeiske, and K. W. Godfrey, [Phys. Rev. Lett.](#) **79**, 2554 (1997).
- ²¹ L. D. C. Jaubert and M. Udagawa, eds., *Spin Ice*, Springer Series in Solid-State Sciences, Vol. 197 (Springer, 2021).
- ²² C. Castelnovo, R. Moessner, and S. L. Sondhi, [Nature](#) **451**, 42 (2008).
- ²³ X.-H. Zhou, Y.-H. Peng, X.-D. Du, J.-L. Zuo, and X.-Z. You, [CrystEngComm](#) **11**, 1964 (2009).
- ²⁴ F. Gándara, F. J. Uribe-Romo, D. K. Britt, H. Furukawa, L. Lei, R. Cheng, X. Duan, M. O’Keeffe, and O. M. Yaghi, [Chemistry - A European Journal](#) **18**, 10595 (2012).
- ²⁵ M. Grzywa, D. Denysenko, J. Hanss, E.-W. Scheidt, W. Scherer, M. Weil, and D. Volkmer, [Dalton Transactions](#) **41**, 4239 (2012).
- ²⁶ J. G. Park, M. L. Aubrey, J. Oktawiec, K. Chakarawet, L. E. Darago, F. Grandjean, G. J. Long, and J. R. Long, [Journal of the American Chemical Society](#) **140**, 8526 (2018), publisher: American Chemical Society.
- ²⁷ M. Grzywa, R. Röß-Ohlenroth, C. Muschielok, H. Oberhofer, A. Błachowski, J. Żukrowski, D. Vieweg, H.-A. K. von Nidda, and D. Volkmer, [Inorganic Chemistry](#) **59**, 10501 (2020).
- ²⁸ J. G. Park, [Nature Chemistry](#) **13**, 11 (2021).

- ²⁹ C.-T. He, Z.-M. Ye, Y.-T. Xu, D.-D. Zhou, H.-L. Zhou, D. Chen, J.-P. Zhang, and X.-M. Chen, *Chem. Sci.* **8**, 7560 (2017).
- ³⁰ L. Sun, C. H. Hendon, S. S. Park, Y. Tulchinsky, R. Wan, F. Wang, A. Walsh, and M. Dincă, *Chemical Science* **8**, 4450 (2017).
- ³¹ B. Javanparast, Z. Hao, M. Enjalran, and M. J. P. Gingras, *Phys. Rev. Lett.* **114**, 130601 (2015).
- ³² A. M. Samarakoon, K. Barros, Y. W. Li, M. Eisenbach, Q. Zhang, F. Ye, V. Sharma, Z. L. Dun, H. Zhou, S. A. Grigera, C. D. Batista, and D. A. Tennant, *Nature Communications* **11**, 892 (2020).
- ³³ D. R. Yahne, D. Pereira, L. D. C. Jaubert, L. D. Sanjeewa, M. Powell, J. W. Kolis, G. Xu, M. Enjalran, M. J. P. Gingras, and K. A. Ross, *Phys. Rev. Lett.* **127**, 277206 (2021).
- ³⁴ S. M. Winter, A. A. Tsirlin, M. Daghofer, J. v. d. Brink, Y. Singh, P. Gegenwart, and R. Valentí, *Journal of Physics: Condensed Matter* **29**, 493002 (2017).
- ³⁵ S. Trebst and C. Hickey, *Physics Reports* **950**, 1 (2022).
- ³⁶ A. M. Hallas, J. Gaudet, and B. D. Gaulin, *Annual Review of Condensed Matter Physics* **9**, 105 (2018).
- ³⁷ J. N. Reimers, A. J. Berlinsky, and A.-C. Shi, *Physical Review B* **43**, 865 (1991).
- ³⁸ B. Canals and D. A. Garanin, *Canadian Journal of Physics* **79**, 1323 (2001).
- ³⁹ A. Gaenko, A. Antipov, G. Carcassi, T. Chen, X. Chen, Q. Dong, L. Gamper, J. Gukelberger, R. Igarashi, S. Isakov, M. Könz, J. LeBlanc, R. Levy, P. Ma, J. Paki, H. Shinaoka, S. Todo, M. Troyer, and E. Gull, *Comput. Phys. Commun.* **213**, 235 (2017).
- ⁴⁰ K. Koepf and H. Eschrig, *Phys. Rev. B* **59**, 1743 (1999).
- ⁴¹ H. J. Xiang, E. J. Kan, S.-H. Wei, M.-H. Whangbo, and X. G. Gong, *Phys. Rev. B* **84**, 224429 (2011).
- ⁴² J. P. Perdew, K. Burke, and M. Ernzerhof, *Phys. Rev. Lett.* **77**, 3865 (1996).
- ⁴³ R. Nath, K. M. Ranjith, B. Roy, D. C. Johnston, Y. Furukawa, and A. A. Tsirlin, *Phys. Rev. B* **90**, 024431 (2014).
- ⁴⁴ M. Creutz, *Physical Review D* **21**, 2308 (1980).
- ⁴⁵ W. Janke, in *Computational Many-Particle Physics*, Vol. 739, edited by H. Fehske, R. Schneider, and A. Weiße (Springer Berlin Heidelberg, Berlin, Heidelberg, 2008) pp. 79–140.
- ⁴⁶ J. F. Greitemann, *Investigation of Hidden Multipolar Spin Order in Frustrated Magnets Using Interpretable Machine Learning Techniques*, Ph.D. thesis, LMU Munich (2019).
- ⁴⁷ F. R. Brown and T. J. Woch, *Physical Review Letters* **58**, 2394 (1987).
- ⁴⁸ M. Creutz, *Physical Review D* **36**, 515 (1987).
- ⁴⁹ D. P. Landau and K. Binder, *A Guide to Monte Carlo Simulations in Statistical Physics, Third Edition*, 3rd ed. (Cambridge University Press, Cambridge, 2009).
- ⁵⁰ D. H. Lyons and T. A. Kaplan, *Physical Review* **120**, 1580 (1960).
- ⁵¹ H. Katsura, I. Maruyama, A. Tanaka, and H. Tasaki, *Europhysics Letters* **91**, 57007 (2010).
- ⁵² K. Essafi, L. D. C. Jaubert, and M. Udagawa, *Journal of Physics: Condensed Matter* **29**, 315802 (2017).
- ⁵³ C. L. Henley, *Physical Review B* **71**, 014424 (2005).